remote sensing

MDPI

Technical Note

Advancing Accuracy in Sea Level Estimation with GNSS-R: A Fusion of LSTM-DNN-Based Deep Learning and SNR Residual Sequences

Yuan Hu [1], Aodong Tian [1], Qingyun Yan [2,*], Wei Liu [3], Jens Wickert [4,5] and Xintai Yuan [4,5]

[1] The College of Engineering Science and Technology, Shanghai Ocean University, Shanghai 201306, China; y-hu@shou.edu.cn (Y.H.)
[2] School of Remote Sensing and Geomatics Engineering, Nanjing University of Information Science and Technology, Nanjing 210044, China
[3] The Merchant Marine College, Shanghai Maritime University, Shanghai 201306, China
[4] The Department of Geodesy, German Research Centre for Geosciences (GFZ), 14473 Potsdam, Germany
[5] Institute of Geodesy and Geoinformation Science, Berlin Institute of Technology, 10623 Berlin, Germany
* Correspondence: qy2543@mun.ca or 003257@nuist.edu.cn

Abstract: The global navigation satellite system reflectometry (GNSS-R) technique has shown promise in retrieving sea levels using signal-to-noise ratio (SNR) data. However, its accuracy and performance are often limited compared to conventional tide gauges, particularly due to constraints in satellite elevation angles. To address these limitations, we propose a methodology integrating Long Short-Term Memory Deep Neural Networks (LSTM-DNN) models, utilising SNR residual sequences as key feature inputs. Our study focuses on the SC02 station, examining elevation angles ranging from 5° to 10°, 5° to 15°, and 5° to 20°. Results reveal notable reductions in root mean square errors (RMSE) of 2.855%, 17.519%, and 15.756%, respectively, showcasing improvements in accuracy across varying elevation angles. Of particular significance is the enhancement in precision observed at higher elevation angles. This underscores the valuable contribution of our approach to nearshore sea level wave height retrieval, promising advancements in the GNSS-R technique.

Keywords: LSTM-DNN; SNR; GNSS-R; different elevation angles; sea level height

check for updates

Citation: Hu, Y.; Tian, A.; Yan, Q.; Liu, W.; Wickert, J.; Yuan, X. Advancing Accuracy in Sea Level Estimation with GNSS-R: A Fusion of LSTM-DNN-Based Deep Learning and SNR Residual Sequences. *Remote Sens.* **2024**, *16*, 1874. https://doi.org/10.3390/rs16111874

Academic Editor: R. Dwi Susanto

Received: 16 April 2024
Revised: 18 May 2024
Accepted: 20 May 2024
Published: 24 May 2024

Copyright: © 2024 by the authors. Licensee MDPI, Basel, Switzerland. This article is an open access article distributed under the terms and conditions of the Creative Commons Attribution (CC BY) license (https://creativecommons.org/licenses/by/4.0/).

1. Introduction

Changes in sea level height are one of the key indicators of global climate change. Through long-term observation of changes in sea level height, the response and trends of the Earth's climate system can be understood, providing data support for climate change monitoring and prediction. Observing the sea level with high temporal and spatial resolution holds immense importance for studying medium and small-scale ocean phenomena. Shore-based sea level altimetry offers a valuable means to obtain sea level height data for monitoring offshore sea surfaces. These data are crucial for understanding ocean dynamics, including currents, tides, and wave patterns, and aid in various applications such as weather forecasting, climate research, and marine navigation. Compared with traditional tide stations, sea buoys, ship altimetry and satellite radar altimetry, GNSS-R sea level altimetry has the advantages of being all-weather and low cost [1]. Since the potential of GNSS-R reflection signals for sea level altimetry has been proposed, it has been one of the hotspots for research by scholars around the world. Global navigation satellite systems (GNSS) have served as indispensable tools for positioning and navigation for several decades. The establishment of the GNSS constellation over 20 years ago marked a significant milestone, opening avenues for various remote sensing applications such as GNSS meteorology [2] and radio occultation [3]. The Global Navigation Satellite System Reflection (GNSS-R) technology predominantly utilises signals from navigation satellites. This method is instrumental in conducting remote sensing operations and in the acquisition

of data pertinent to various surface parameters. It has many applications in, e.g., sea level monitoring [4,5], snow depth detection [6], soil moisture retrieval [7], sea ice thickness estimation [8,9] and vegetation water content observation [10].

From its initial explorations in sea level monitoring to the augmentation of theoretical understanding, GNSS-R technology has evolved into a mature and valuable tool. GNSS satellites continuously transmit, while travelling from the satellite to the receiver, radio transmissions with multipath of mistakes in the radio signal. One of the mistakes that impediments might cause is multipath in the vicinity of the receiver, which causes a signal delay through the signal's reflection before it reaches the receiver antenna. Although multipath is considered as a source of error in GNSS position, it is regarded as a legitimate dataset that includes details about the GNSS-R's reflective surface. By observing the temporal variation in the geometric distance between the GNSS antenna and the specular reflection point on the water surface, the temporal variation in the water level can be observed. In 1993, Martin-Neira pioneered the application of combining direct and reflected signals for ocean altimetry, introducing the concept of PARIS (Passive Reflectance and Interferometry System) [11]. Building upon this, Anderson in 2000 proposed the utilization of GPS signals for early determination of water levels and tidal variations [12]. These experiments demonstrate that the reflected signals can carry valid physical information about the reflecting mirror surface, and that the corresponding physical information about the surface can be inversely performed using the interferometric signals.

As technology advances, more and more new techniques are being used for sea level inversion. In 2022, Nutpapon Limsupavanich et al. [13] for the first time used recurrent neuron networks (RNNs) to train a signal-to-noise ratio (SNR) noise model, which was utilised to remove noise from SNR signals. The experimental findings indicated that employing RNN for SNR denoising led to a decrease in the root mean square error (RMSE) by 3 cm compared to the prior approach and a reduction of 9 cm in comparison to denoising utilising the empirical mode decomposition (EMD). In scenarios necessitating brief SNR data, RNN-based denoising methods demonstrate superiority over EMD techniques. In 2021, Su-Kyung Kim et al. [14] used multi-constellation, multi-frequency GNSS-R observations to derive the principle that water levels should be consistent from multi-frequency signals on a single ray path and then combined this with random sample consensus (RANSAC) and the least squares method to efficiently filter out a large number of unreliable data points in order to effectively measure the extreme changes in water levels during storm surges. In order to predict the absolute sea level at two locations in Australia (Port Kembla and Milne Bay), Nawin Raj et al. [15] combined a convolutional neural network (CNN) with a bi-directional long-short-term (BiLSTM) model with successive variational mode decomposition (SVMD) in 2023. This model produced better results than multi-layer perceptrons (MLP), support vector regression (SVR) and gradient boosting (GB). In experiments, the results showed that the SVMD-CNN-BiLSTM model achieved the highest values for the Willmott index, Nash–Sutcliffe index, and Legates and McCabe indices for both sites. The predicted linear trend indicates that the annual mean sea level in 2030 will rise. In 2023, Jian et al. [16] analysed and explained that conventional methods do not adapt well to the extraction of SNR residuals as the elevation angle increases. The problem of false peaks occurs when using spectral analysis, making the inversion results distorted. In order to solve this, some scholars have used empirical modal decomposition and variational modal decomposition (VMD) to reconstruct the SNR residual sequence to eliminate the distortion of inversion results [17]. Conventional spectral analysis leads to distorted inversion results due to the gradual decrease in the interfering signal components as the elevation angle increases. However, the ensuing sequence of SNR residuals should not be misconstrued as an indication of the absence of prospects for accurate inversion at elevated angles. On the contrary, these residuals may still harbour the potential for precise inversion, notwithstanding the increased elevation angle.

The proposed strategy in this study is concerned with the stability and accuracy of retrieval in different elevation ranges. Furthermore, deep learning has greater robustness

and accuracy and may perform well in sea surface elevation retrieval. Therefore, this paper proposes to use the GNSS-R extracted SNR residual sequences as input parameters to the model. This methodology proves advantageous in addressing the complexities associated with land subsidence and obviates the necessity for recurrent adjustments of antenna elevation. It exhibits enhanced resilience across a range of elevation angles and circumvents the distortion of inversion outcomes during spectral analysis, which is attributable to the incremental attenuation of interfering signal oscillations concomitant with an increase in the elevation angle. In order to verify the conjecture of the above method, we chose the SC02 station for the experiment. Section 2 describes the traditional sea level retrieval method, quality control, LSTM-DNN model and the flow scheme of the proposed strategy. Section 3 details the data information. Section 4 presents the reflection point area analysis, the comparison analysis between the proposed method and the conventional method. And we discuss the applicability of the method to regular and irregular waves in Section 5. Finally, we draw conclusions in Section 6.

2. Sea Level Inversion Approach

2.1. The Principle of GNSS-IR Technology

As depicted in Figure 1, concerning the geometric configuration in GNSS-R, the GNSS receiver captures both the direct signal emitted by the satellite and the reflected signal from the reflecting surface. In the figure, the symbol for the angle between the reflected surface and the direct signal is θ, while the height of the antenna phase center to the reflective surface is denoted by RH. TG is the tide gauge, Hs is the height from the phase centre of the antenna to the datum of the tide gauge, and h is the height of the sea level. Direct and reflected signals interfere with one another during the satellite electromagnetic wave propagation process, and this coherence phenomena will be reflected in the change in the received SNR [18]. In GNSS observations, the acquired data serve as a valuable input for deducing the sea level height through inversion. The oscillation component, stemming from the multipath effect, encapsulates the pertinent physical details of the reflecting surface. This characteristic enables the extraction of the sea level height and additional parameters related to the surrounding medium.

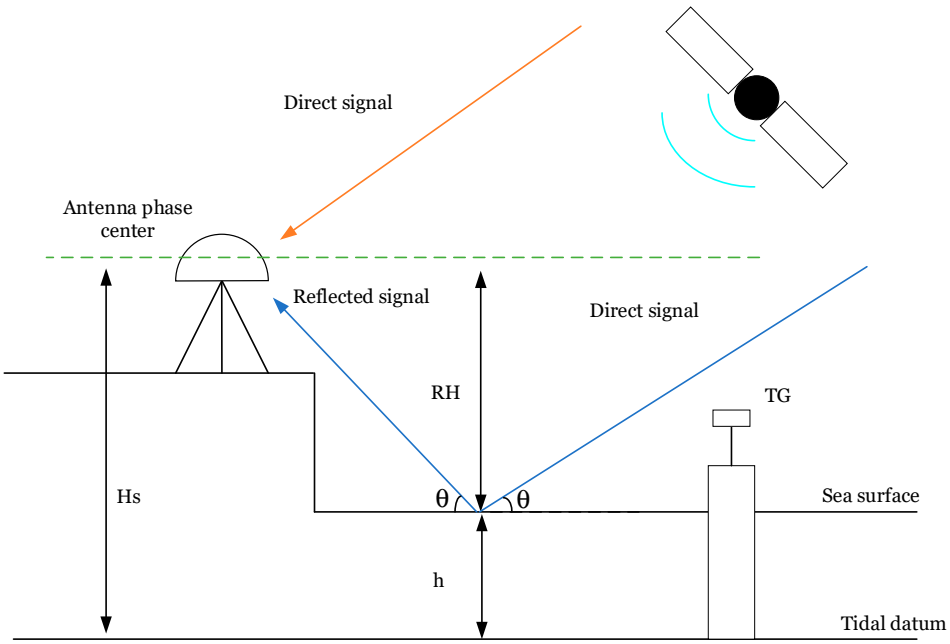

Figure 1. The geometry of the GNSS-IR tide level monitoring system situated on land.

When electromagnetic waves propagate to produce an SNR signal, the multipath effect is known as [19]:

$$SNR = (I_d + I_r + I_r^l)/I_n + 2\sqrt{(I_d I_r)}cos(r_i)/I_n \quad (1)$$

where SNR is the interference signal, I_d is the direct signal power, I_r is the reflected signal power, I_n is the noise signal power, and I_r^l is the incoherent signal power, ρ_i is the interferometric phase. When I_d is much larger than I_r, the trend term in the SNR interferometric signal can be removed by an appropriate method, usually using a polynomial fit to remove that trend term. Given that the trend term does not substantially contribute to sea level inversion, its removal is warranted, thereby preserving the oscillatory component of the signal [20]. In the context of academic writing, the multipath frequency modulates of SNR_{osc} are as follows:

$$SNR_{osc} = A\cos\left(\frac{2\pi}{\lambda}D + \varphi\right), \quad (2)$$

where A is the oscillation amplitude, φ is the initial phase of the multipath oscillation term, and λ is the wavelength. $D = 2RHsin(\theta)$ can be derived from the geometric relationship in Figure 1 [21]. The phase difference γ of the SNR_{osc} that is impacted by multipath is [22]

$$\gamma = \frac{2\pi}{\lambda}D = \frac{4\pi RH\sin(\theta)}{\lambda} \quad (3)$$

To assess the frequency, Lomb–Scargle periodogram (LSP) analysis is used, the frequency can be calculated as follows:

$$2\pi f = \frac{d\gamma}{d\sin(\theta)} = \frac{4\pi RH}{\lambda} \quad (4)$$

RH can be obtained as a function of frequency [23,24].

$$RH = \frac{f\lambda}{2} \quad (5)$$

Ultimately, the derived result is the determination of sea level height [6].

$$h = Hs - RH \quad (6)$$

When subjected to LSP spectral analysis, the computation of the vertical distance from sea level to the antenna's phase centre is feasible. However, this method in isolation is insufficient for determining the optimal height of the reflector. It is imperative to integrate additional data or apply supplementary analytical techniques to refine the reflector height estimation for enhanced accuracy. For example, when the SNR signal screening requirements are as follows: elevation angles in the range of 5°–12° and azimuths in the range of 0°–360°. Figure 2 shows the results of the LSP spectral analysis of day of year 1 (DOY1), L1-band GPS-5 at SC02 station in 2021 and the estimated DOY1–DOY3 reflector heights. Figure 2a,b show the results of the spectral analysis of GPS PRN5 obtained at different times of the day. The 6:11 time point corresponds to a reflector height (RH) of 0.875 m, and 10:56 and 00:33 correspond to 1.24 m and 1.08 m, respectively. Figure 2c–e show plots of reflector height with time for the three days of DOY1–DOY3 in 2021, and the colour bars corresponding to the satellite bands, azimuths and amplitudes of the LSP spectral analysis are shown on the right, respectively. Inadequate filtering of the SNRs can indeed lead to suboptimal inversion outcomes. For instance, as illustrated in Figure 2d, the presence of dark- and light-coloured inversion points at the upper section is observable. These points are indicative of low and high azimuths, respectively, with north being represented as 0° and increasing in a clockwise direction. The corresponding values are reflective of signals emanating from terrestrial sources, which are extraneous to the desired ocean surface reflections. Such land-based signals are not the target of the inversion process, and

therefore, measures should be taken to differentiate and exclude them from the analysis to avoid contamination of the results. Therefore, it is crucial to implement robust filtering techniques to isolate the genuine signal and enhance the quality of the inversion results. This process is essential for ensuring the reliability and precision of the data derived from the spectral analysis. According to [25,26], the measured sea level height needs to be harmonised with the tide gauge datum in order to validate the comparison, i.e., obtained to Hs. Typically, the sampling frequency of a tide gauge differs from that of GNSS. To ascertain the instantaneous sea level at the precise moment via GNSS, it is advisable to implement a linear interpolation method. This technique will enable the synchronization of data between the two systems, ensuring that the sea level readings are accurately aligned with the GNSS timestamps. The practical application of this method and its efficacy will be further elucidated in the experimental section of the study. The derivation of continuous sea level height measurements may exhibit significant discrepancies when compared with tide gauge data. Beyond the apparent wave-like pattern of the inversion, there are some abnormal spots in the upper part, which may be due to the reflection of electromagnetic waves on land, etc. [27]. Consequently, the spectral analysis procedure necessitates rigorous QC to ensure the integrity and accuracy of the results. This QC is essential to filter out noise and anomalies, thereby refining the data for more reliable sea level height estimations. The specific QC implementation for the SC02 station is as follows:

1. pknoise > 2.8. The maximum amplitude should be 2.8 times larger than the average background noise amplitude.
2. maxAmp > 5. Maximum amplitude peak in LSP spectral analysis should be greater than 5.
3. 3 m < RH < 12 m. The effective reflector height at SC02 station should be between 3 m and 12 m.
4. $\Delta elevation \geq 5^{\circ}$. The difference between the maximum and minimum values of the elevation's angle is at least 5°.
5. ArcdelT < 75. The maximum duration of SNR_{osc} data used for inversion should not exceed 75 min.

The QC criteria given in this study are the better QC criteria based on the SC02 station experiment. Different stations will receive different QC standards after experimentation. In addition to this, it is also considered that tropospheric delays can cause proportional errors in the measured reflector heights to the true geometric heights. A global pressure temperature 2 wet (GPT2w) model [28] is combined with astronomical refraction [29] to correct for tropospheric delay according to Peng et al. [30]. This elevation angle correction can be described as follows:

$$\Delta\theta = \frac{510}{492 + \frac{9T}{5}} \times \frac{P}{1010.16} \times \frac{1}{\tan(\theta + \frac{7.31'}{\theta + 4.4^{\circ}})} \tag{7}$$

where θ in units of degree, $\Delta\theta$ in units of minute, T the temperature in units of Celsius degree, and P is the pressure in a unit of hPa. The constraints on the azimuth angle according to Figure 2d will also have an effect on the inversion results, so the appropriate azimuth angle should be selected based on google maps or satellite images. Outliers should usually be removed before obtaining the sea level height, but this study aims to investigate the advantages and disadvantages between the proposed strategy and the conventional methods, so the outlier detection will be shown in the experimental part, but the results are not considered.

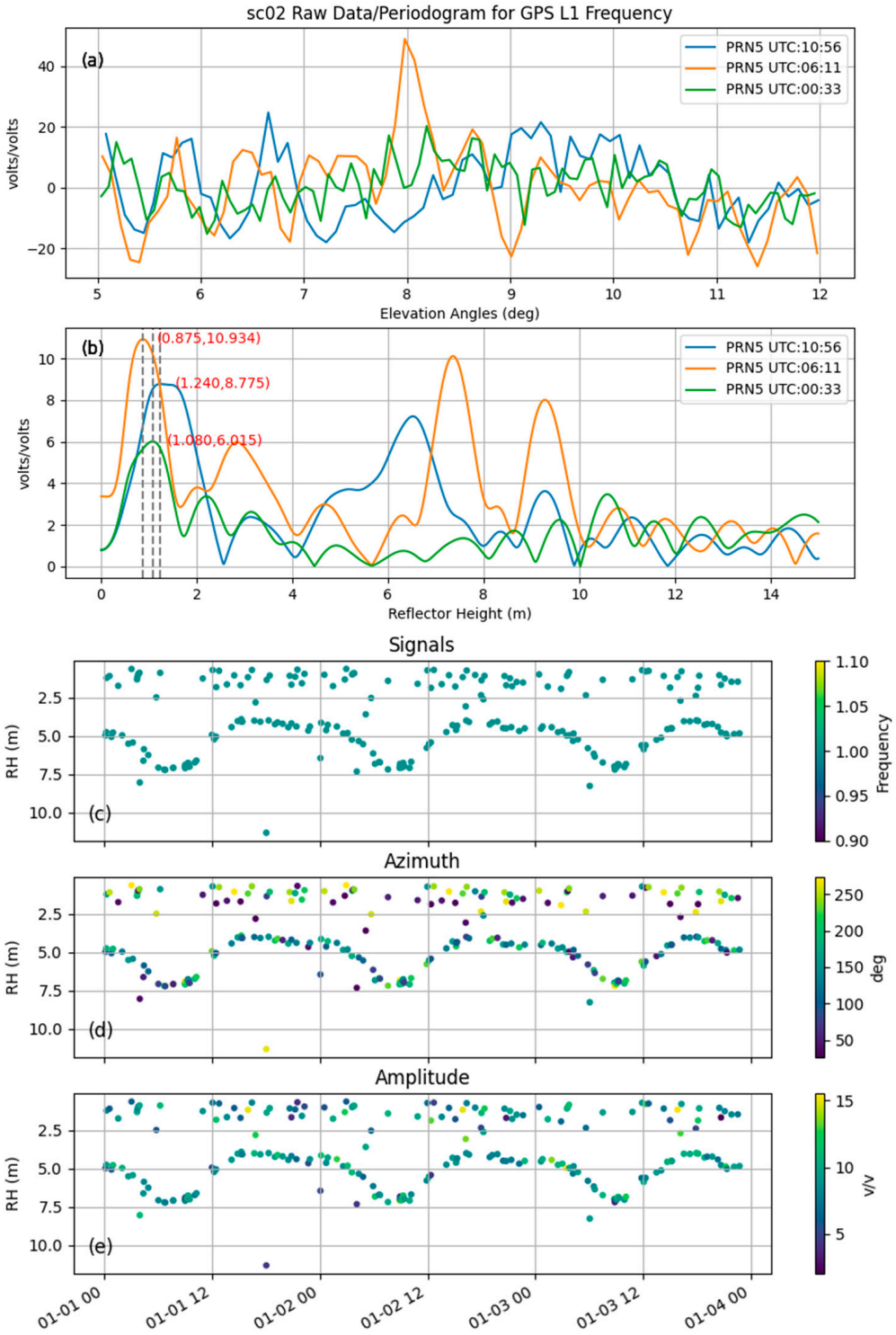

Figure 2. (**a**,**b**) are the SNR residual sequences as well as the spectral analysis plots, and (**c**–**e**) are the RH inversion results of DOY1–DOY3 for the year 2021. The colour bar is the satellite bands, azimuths, and magnitudes of spectral analyses from the top to the bottom, respectively.

2.2. The Principle of LSTM

LSTM, a variant of recurrent neural network (RNN) architecture, is specifically crafted to overcome the challenges associated with capturing long-term dependencies in sequential data. Conventional RNNs often grapple with issues such as vanishing gradients, where the gradients dwindle during backpropagation through time [31]. This phenomenon results in learning difficulties and an inability to retain information across extended sequences. LSTM introduces an intricate structure featuring gated mechanisms that regulate the information flow. The model comprises three pivotal gates: the input gate, the forget gate, and the output gate. Each gate employs a sigmoid activation function to yield values between 0 and 1, dictating the degree of openness for that gate. Furthermore, LSTMs integrate a hyperbolic tangent (tanh) activation function to generate a candidate value. The processing flow of LSTM is as follows:

$$\begin{aligned} i_t &= \sigma(W_i[h_{t-1}, x_t] + b_i) \\ f_t &= \sigma(W_f[h_{t-1}, x_t] + b_f) \\ o_t &= \sigma(W_o[h_{t-1}, x_t] + b_o) \\ \widetilde{C}_t &= \tanh(W_c \cdot [h_{t-1}, x_t] + b_c) \\ C_t &= f_t \cdot C_{t-1} + i_t \widetilde{C}_t \\ h_t &= o_i \cdot \tanh(C_t) \end{aligned} \tag{8}$$

where σ is the activation function, W and b are the weight coefficient and bias function, respectively. $\widetilde{C}_t$ and C_t are the candidate value at time t and memory cell state at time t. *tanh* is the hyperbolic tangent activation function. x and h are the current input and output information, respectively. These equations depict the flow of information through an LSTM unit, showcasing how it selectively updates, forgets, and outputs information, allowing for more effective handling of long-term dependencies in sequential data.

2.3. Inversion Process of Proposed Strategy

The SNR interferometric signals of the GPS L1 band were filtered by selecting elevation, azimuth and quality controlling before removing the trend term by quadratic fitting. The de-trended residual sequences include all samples of the training and test sets (i.e., 2018 to 2021), searched for the longest arc length value in them (Max_n) and then interpolated for each SNR residual sequence sample. The interpolated SNR residual sequences have the same dimension, and then, the SNR residual sequence samples are normalised to divide the dataset for comparison with the tide gauge by LSTM-DNN model prediction. The experiment used the LSTM-DNN model compared with the conventional method (CM) to inverse the SC02 station. The normalization formula is described as follows:

$$X = \frac{x - x_{\min}}{x_{\max} - x_{\min}} \tag{9}$$

where X is the normalised value of the feature $\in$ (0,1), x is the original value of a feature, x_{max} is the maximum value of that feature among all samples, and x_{min} is the minimum value of that feature in all samples. The specific flow chart is shown in Figure 3.

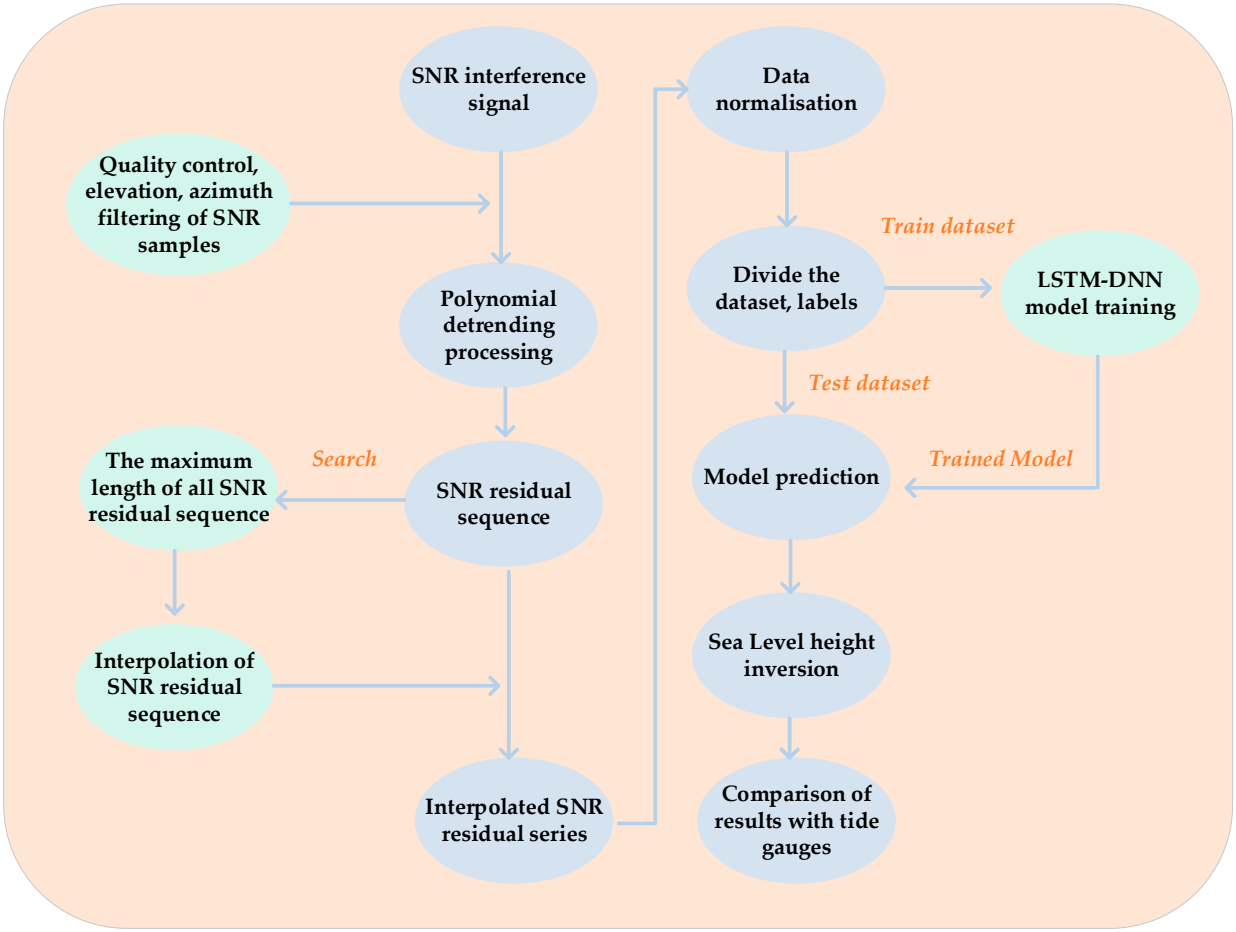

Figure 3. Flow chart of sea level inversion.

3. Dataset Information

Station SC02, situated at 48.5°N, 123.0°W, in Friday Harbor on the west coast of the United States, is managed by the University Navstar Consortium. The global location coordinates are depicted in Figure 4, with the red star indicating the station's precise location. To validate the proposed feasibility, datasets were gathered for SC02 from 2018 to 2021. The GNSS data spanning from 2018 to 2020 will serve as the training set for the model, while the data from 2021 will be utilised as the test set. A Trimble TRM29659.00 antenna with a SCIT radome is part of the station's equipment. It is connected to a Trimble NETRS GPS receiver, which records data at 15 s sampling intervals. The antenna is situated at a height of roughly 5.5 ± 2.3 m above sea level. To ensure that the reflected signals originate from the open ocean and to mitigate the effects of land reflections, signals within an azimuthal range of 60° to 220° were analysed. A tide gauge (TG) operated by the National Oceanic and Atmospheric Administration (NOAA) is positioned 300 m west of station SC02. Sea level observations at 6 min intervals from this tide gauge were collected as reference data for the year 2021. Tidal datum data were obtained using mean lower low water (MLLW).

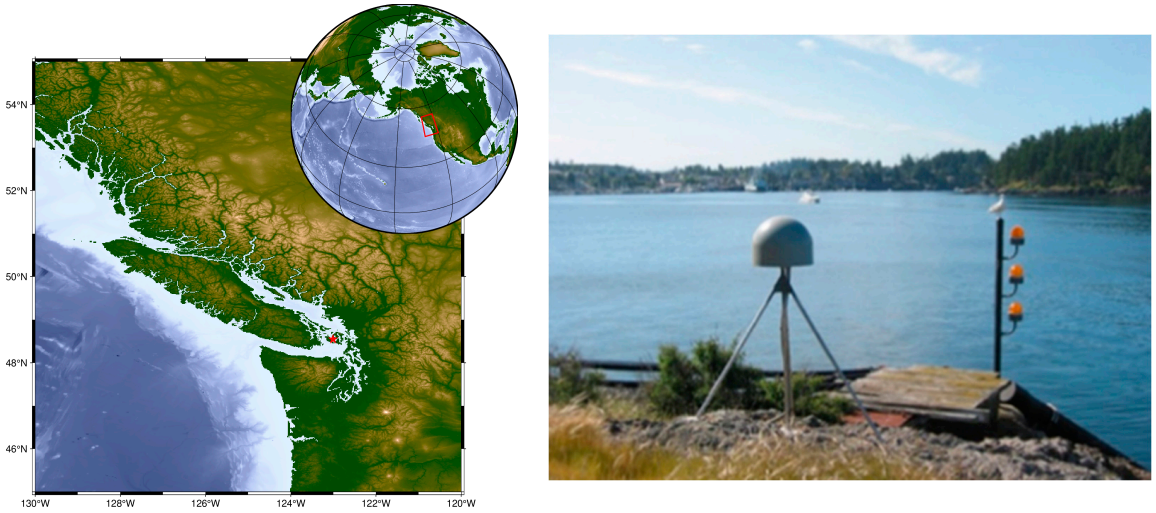

(**a**) (**b**)

Figure 4. SC02 station information: (**a**) SC02 geographic location; (**b**) SC02 station receiver and surroundings.

4. Experimental Results

4.1. Station SC02 Fresnel Reflectance Region and Model Evaluation Criteria

This experimental study utilises the inversion results of 2021 at different elevation ranges using the GPSL1 band at site SC02, divided into the cases of 5°–10°, 5°–15° and 5°–20°. The azimuth angle of 60°–220° was selected based on Google maps, which is able to encompass most of the water surface to ensure that the satellite reflection signal can be reflected on the water surface. The Fresnel zone is the region of constructive reflection accumulation that encircles the reflection point of the Ray Theory [32]. Figure 5 shows the Fresnel zone at site SC02, which corresponds to elevation angles of 20°, 15°, 10° and 5° from inside to outside, respectively (green, red, blue and yellow areas). A high elevation angle corresponds to an area of the sea that is closer to the shore and is called a near-shore area. The lowest and highest tide levels measured at the tide gauge in Friday Harbour in 2021 were −1.043 m and 3.150 m. The lowest and highest tide levels at the tide gauge corresponded to effective reflector heights of 7.858 m and 3.665 m, respectively, with an average effective reflector height of 5.7615 m. Figure 5a–c are referenced to the house in the upper left corner, respectively, and it is clear to see that the radius of the first Fresnel reflection region increases as the height of the reflector increases, and from that analysis, the radius of the first Fresnel reflection region becomes smaller with the high tide and larger with the low tide.

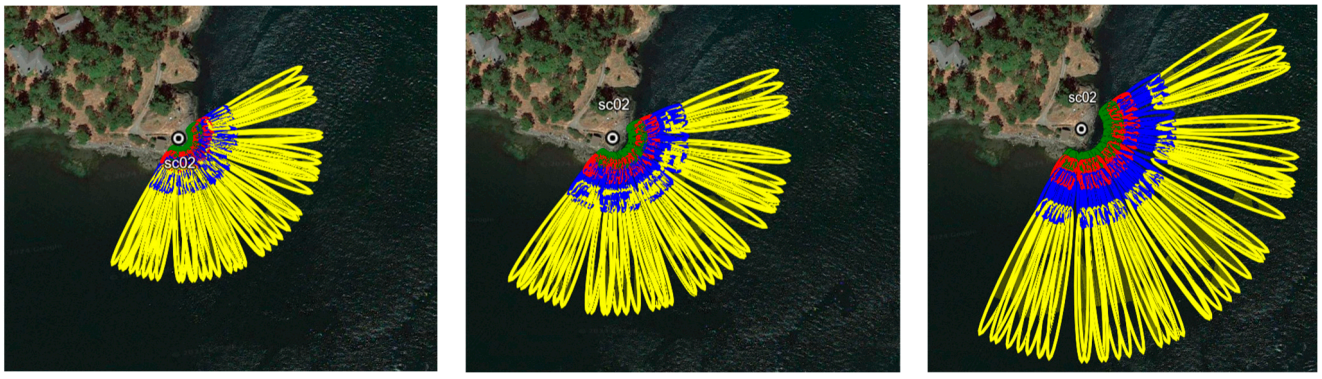

(**a**) (**b**) (**c**)

Figure 5. First Fresnel Reflection Zone at SC02 station with elevation angle of 20°, 15°, 10°, 5° of DOY 1 in 2021. The figures (**a**–**c**) correspond to RH = 3.665 m, 5.7615 m, 7.858 m, respectively.

In order to describe more accurately the distance between the satellite reflector point and the station, Figure 6 demonstrates the distance from the satellite reflector point to the station when the height of the reflector is 3.665 m, 5.7615 m and 7.858 m. The figure shows the position of the satellite relative to the station at the point of reflection for a given calendar element, with the x and y axes indicating straight-line distances in the east–west and north–south directions, respectively, centred on the station. The equation for the straight-line distance between each reflection point and the station is expressed as follows:

$$dis = \frac{RH}{\tan(\theta)} \tag{10}$$

where *dis* is the distance between the station and the reflection point. The maximum and minimum values of *dis* are the corresponding minimum and maximum elevation angle, respectively. The station boasts maximum straight-line distances of 41.89 m, 65.85 m, and 89.82 m, accompanied by elevation angles of 5°. At these distances, the corresponding RH are 3.665 m, 5.7615 m and 7.858 m, respectively. And the minimum straight-line distances are 10.07 m, 15.83 m and 21.59 m, accompanied by elevation angles of 20°. The chosen geographical area for sea level inversion in this study is a sector centred on the station, with radii corresponding to both the minimum and maximum distances. Notably, it was observed that the trajectories of reflection points exhibited a gradual increase in both maximum and minimum distances with the rising reflection height. Furthermore, the rate of increase in maximum distance outpaces that of the minimum distance, indicating that the reflection zone tends to contract during high tide and expand during low tide, aligning with the findings presented in Figure 5. In order to use the available satellite signals for sea-level inversion on as wide a scale as possible, a quality control measure was implemented that required variations of more than 5° between the maximum and minimum elevation angles of the satellites.

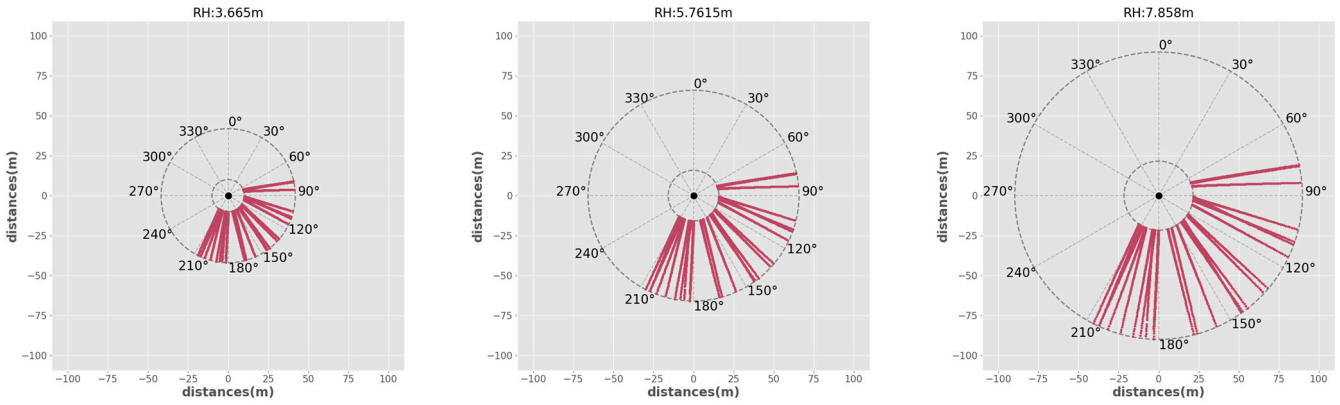

(**a**) (**b**) (**c**)

Figure 6. Satellite reflection points trajectory diagram of SC02 for DOY2 in 2021. The figure (**a**–**c**) correspond to RH = 3.665 m, 5.7615 m, 7.858 m, respectively.

In this study, the SC02 station served as the focal point for sea level inversion. The study entailed a comparative analysis of accuracy assessment parameters alongside tide gauge data across various elevation range scenarios. Additionally, an error analysis was conducted to contrast the CM with the proposed strategy, again using tide gauge data for different elevation ranges as a benchmark. The precision of the sea level inversion was evaluated using key statistical metrics: the coefficient of determination (R^2), root mean square error (RMSE) and mean absolute error (MAE). The sample standard deviation of the difference between the values that were seen and those that were predicted is represented by RMSE. The RMSE in order to indicate the degree of dispersion of the sample. MAE denotes the mean of the absolute errors between predicted and observed values, whereas

RMSE penalises high variances more compared to MAE. R^2 denotes an evaluation metric for the assessment of linear models.

4.2. Sea Level Inversion at Different Elevation Ranges

In order to validate the proposed strategy, this section presents the performance metrics of GPS band L1 across different elevation ranges. The QC procedures outlined in Section 2.1 are effective in the exclusion of anomalies that may arise from ground reflections or obstructions. Furthermore, azimuthal control is employed to guarantee that the signal reflection points are confined to the sea surfaces. Additionally, amplitude control, coupled with a threshold stipulating that the peak value must exceed the background noise by a factor of 2.8, is implemented to filter out invalid inversion results. These measures collectively ensure the validity and reliability of the sea level inversion points derived from the data. Figure 7 shows the results of the sea level inversion for one year, from top to bottom corresponding to elevation ranges of 5°–10°, 5°–15°, and 5°–20°, respectively, with the red translucent portion being the zoomed-in area of the section. It can be seen that in the elevation range of 5°–10°, the GNSS inversions basically coincide with the tide gauge data, but there are still some days when the GNSS inversions are 1–2 m away from the tide gauge data, which is partly reflected in the high tide level. The high tide level also corresponds to a lower reflector height. From the analysis of Figure 6 above the satellite reflection point is close to the straight-line distance from the station when the reflector height is lower, which also indicates that the traditional spectrum analysis method of inverting the sea level height is not very effective when the tide is high in the near-coastal area. In the case of 5°–15°, 5°–20°, with the increase in the upper limit of elevation angle, there appeared to be some low tide part of the poor effect of the inversion value (there are some inversion values below −1 m from the case of Figure 8 CM5-20). Although the low tide level corresponds to higher reflector heights, the satellite reflection points at high elevation angles also occur in areas near the coast. In this case, it is possible that the inversion values at higher reflector heights are biased by the increasing elevation angle, which causes the oscillation of the SNR residual series to become less pronounced and therefore biased in the spectral analyses. There are obvious oscillations in the SNR residual sequence from 5° to 12° in Figure 7a, and the oscillations are significantly weakened at 14°–17° leading to distortion in the LSP analysis results. At this time, the difference between TG and the spectral analysis in Figure 7b is 2.123 m. If the SNR residual sequence is taken as 5°–15°, the RH of spectral analysis is 7.06 m, while the corresponding RH of TG is 6.85 m. The difference is 0.21 m.

In order to circumvent the shortcomings of the spectral analysis, the proposed strategy is able to invert the sea level height well over a range of elevation angles. The LSTM-DNN structure network is shown in Table 1. The optimiser of LSTM-DNN is Adam, the loss function is the mean square error, dropout is 0.1, learning rate is 0.00001, batch size is 32, and the activation function is the Rectified Linear Unit (ReLU).

Figure 9 shows the LSTM-DNN inversion of sea level height for one year. From the figure, it can be clearly seen that the LSTM-DNN inversion values obtained at both low and high tide levels fit the tide gauge data when the upper limit of elevation varies at different elevation angles. According to the above analysis, the poor accuracy after spectral analysis due to the weakened oscillation of the SNR parameter sequence at high elevation ranges is improved here, indicating that the SNR residual sequence still has the potential to invert the sea level height when the elevation angle increases. This also corrects the poor inversion values for some of the near-coastal reflection points.

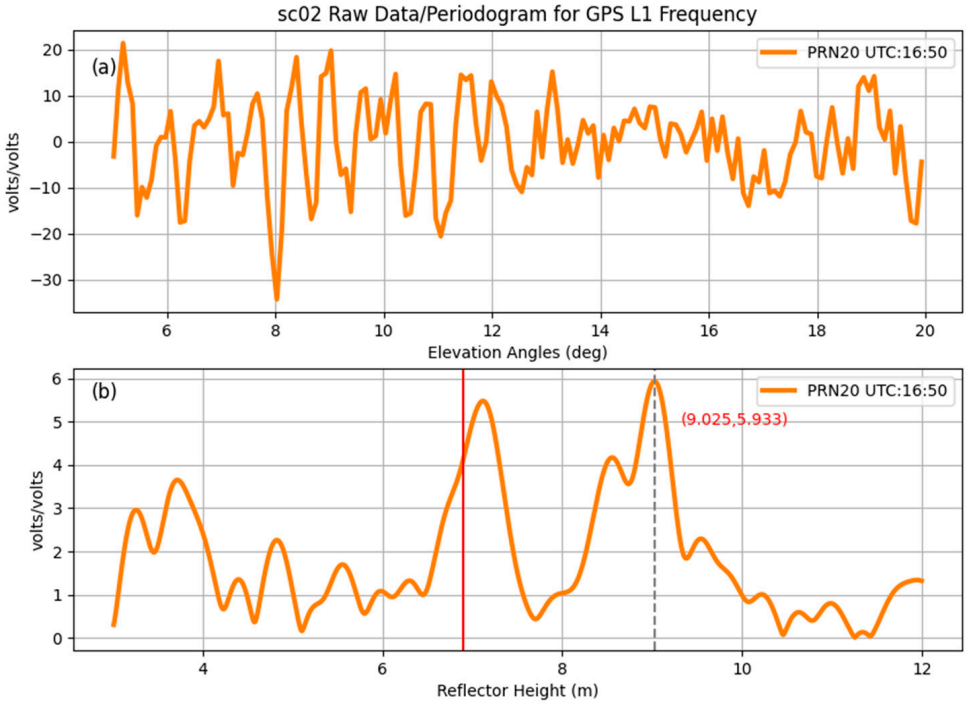

Figure 7. (**a**) is the SNR residual sequence of GPS PRN20 on 10 July 2021, at 16:50:14 of the same day, and (**b**) is the LSP spectral analysis plot, with the red vertical line showing the TG corresponding to the reflector height of 6.902 m, and the grey vertical dashed line showing the reflector height of 9.025 m for the spectral analysis.

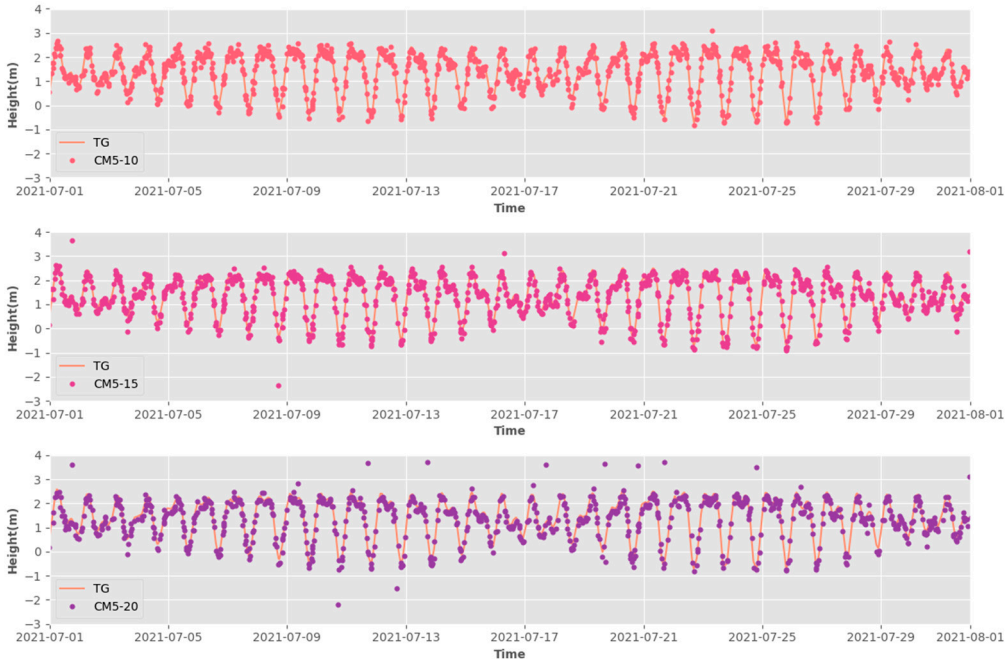

Figure 8. CM sea level inversion results for one of the months in 2021. From top to bottom are the results of the elevation range 5°–10°, 5°–15° and 5°–20°, respectively.

Table 1. LSTM-DNN structure.

Mould	Layer	Value
LSTM-DNN	Lstm1	(Max_n, 128)
	Dnn1	(128, 64)
	Dnn2	(64, 32)
	Dnn3	(32, 1)

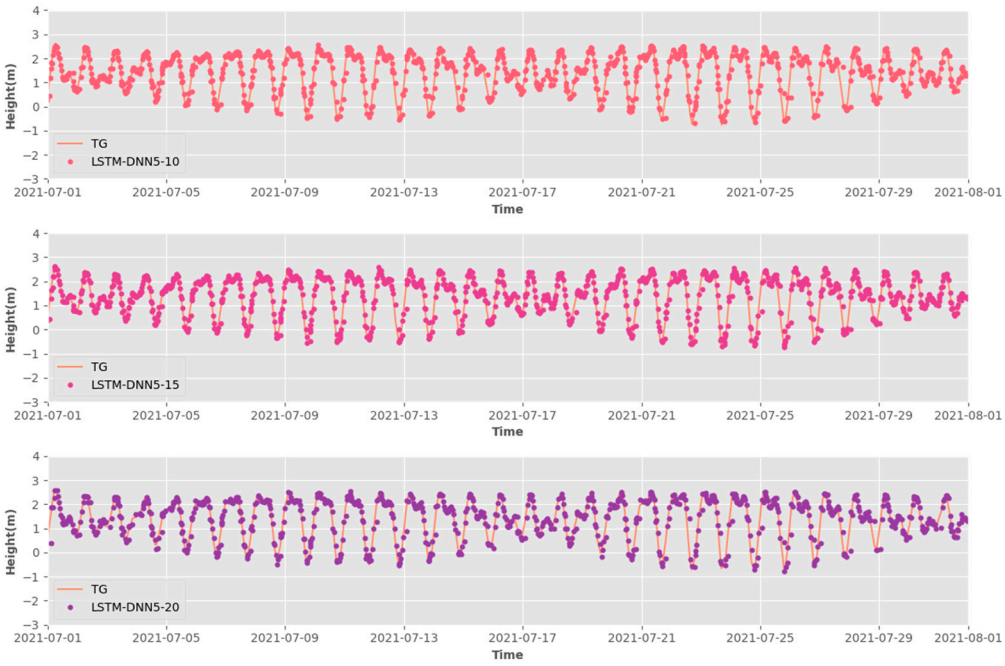

Figure 9. LSTM-DNN method sea level inversion results for one of the months in 2021. From top to bottom are the results of the elevation range 5°–10°, 5°–15° and 5°–20° LSTM-DNN methods, respectively.

Quartiles and box plots are commonly used to detect outliers and can assess the data dispersion. As depicted in Figure 10, the box plots for the two methodologies across varying elevation angle ranges reveal distinct patterns. The outliers under the CM are notably more clustered within the 5°–10° range. In contrast, for the elevation ranges of 5°–15° and 5°–20°, the outliers are more evenly distributed. Furthermore, a comparative analysis of the six results indicates that the CM outcomes exhibit greater dispersion, whereas the LSTM-DNN results are more tightly grouped. The median value for the LSTM-DNN is marginally elevated in comparison to the CM, suggesting a potential shift in the overall trend towards higher tide levels. This observation could be indicative of the LSTM-DNN's enhanced capability to capture the high tide signal more effectively than the CM. The Van de Casteele diagram, as presented in Figure 11, serves as a graphical representation to compare the GNSS inversion values with tide gauge data. The horizontal axis quantifies the discrepancy between the GNSS-derived sea level and the tide gauge measurements, while the vertical axis represents the tide gauge data itself. The diagram evidently illustrates that a majority of the inversion values align with periods of high tide. Moreover, it is discernible that the LSTM-DNN method yields inversion values that are more closely aggregated around the zero-difference mark compared to the CM, indicating a higher precision in sea level estimation by the LSTM-DNN approach. This convergence towards zero suggests that the LSTM-DNN method may provide a more accurate reflection of the tide gauge data, thereby offering potential improvements over the CM in sea level inversion accuracy. The results presented in Table 2 indicate that the LSTM-DNN model exhibits consistent performance in the elevation ranges of 5°–10° and 5°–15°, with an RMSE of approximately 17 cm for both. For the elevation range of 5°–20°, the RMSE increases slightly to 21.227 cm.

Compared to the CM, the LSTM-DNN model enhances accuracy, reducing the RMSE by 2.855%, 17.519%, and 15.756% across the respective elevation ranges. Similarly, the MAE shows an improvement in accuracy by 12.655%, 18.778%, and 11.934% for each elevation range, respectively. The experimental data from the three elevation range groups reveal that the accuracy enhancement is marginal within the 5°–10° range, whereas the other two ranges demonstrate a more pronounced improvement. This underscores the robustness of the LSTM-DNN method for sea level height inversion, particularly highlighting its efficacy in the inversion of near-coastal regions. The improved accuracy in these areas is indicative of the method's potential for reliable sea level monitoring, which is critical for coastal management and environmental studies.

Table 2. Sea level inversion results.

Method	Elevation	R^2	RMSE	MAE
CM	5°–10°	95.20%	17.937 cm	14.158 cm
	5°–15°	93.71%	20.843 cm	15.615 cm
	5°–20°	90.83%	25.197 cm	17.614 cm
LSTM-DNN	5°–10°	95.23%	17.425 cm	11.888 cm
	5°–15°	95.49%	17.191 cm	11.701 cm
	5°–20°	93.19%	21.227 cm	14.607 cm

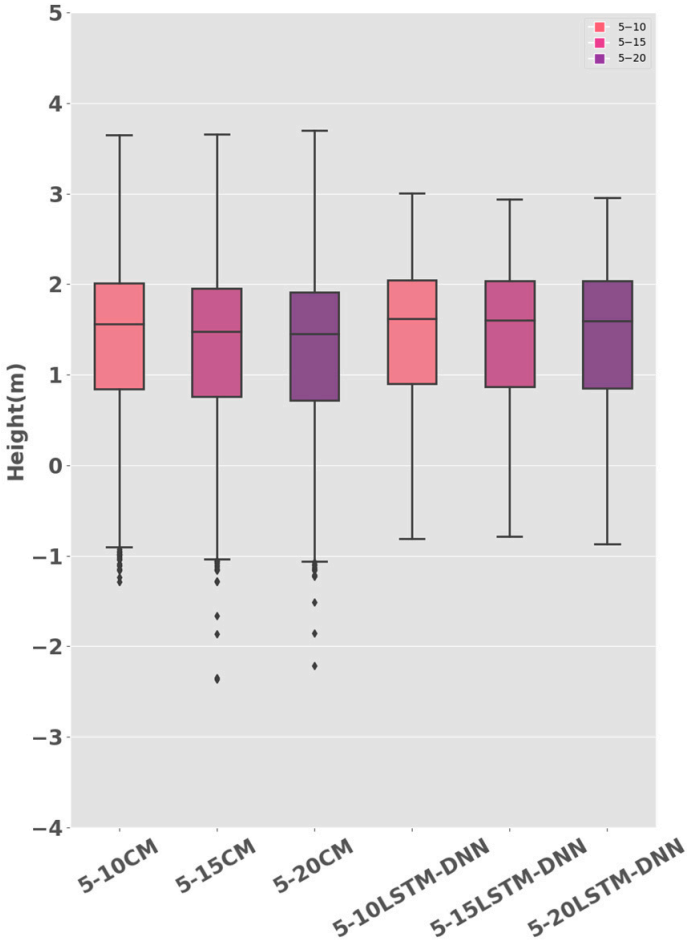

Figure 10. Box plots of the two methods for different elevation ranges.

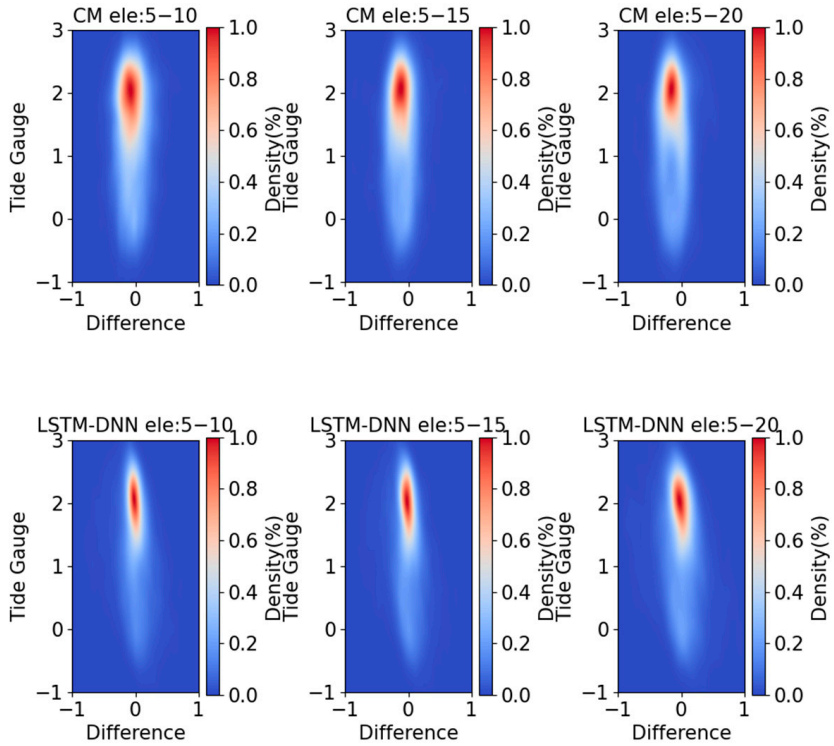

Figure 11. Van de Casteele diagram for different elevation ranges.

5. Discussion

The article comprehensively analyses the methodology of sea level estimation using LSTM deep learning networks to analyse the sea state with regular fluctuations, such as the sea state at station SC02. However, there is a lack of more in-depth discussion and research on cases involving irregular fluctuation patterns such as tsunamis. Bayındır et al. [33], Xu and Wu [34], and Meng et al. [35] conducted an in-depth study on the prediction of tsunami waves and prolonged wave sequences by using a time series model such as LSTM. In the case where both normal and solitary waves (tsunami waves) coexist above a slowly changing tide level, the LSTM-based approach of the above et al. adapts to this situation by learning from historical tide data. GNSS-R sea surface altimetry changes its interferometric signal SNR accordingly when the sea state changes, and by training the network on a GNSS dataset that contains a variety of sea states with both normal and irregular fluctuation patterns, the LSTM model is able to capture the underlying dynamics affecting sea level fluctuations. This adaptation may allow the model to provide more robust estimates and more reliable predictions. For solitary waves (tsunami waves), Xu and Wu discovered that adding Convolutional Neural Networks (CNN) to LSTM (forming CNN-LSTM models) effectively extracts tsunami features. Therefore, combining CNN with LSTM-DNN models can enhance the extraction of tsunami features and fuse with SNR oscillatory terms to better invert the sea state for solitary waves, increasing the model's utility in various practical applications.

6. Conclusions

In this paper, the SC02 station was tested, and different results were obtained for different elevation angle ranges. It can be found that the LSTM-DNN model possesses good robustness over CM in the case of long-time inversion. Especially as the upper elevation limit increases, the residuals of station SC02 are lower than CM, respectively, which indicates that the fitting effect is better and matches the tide gauge data very well. Simultaneously, this enables the direct inversion of the sea surface height by deep learning with the SNR residual series. The LSTM-DNN model exhibits great accuracy in the sea

level retrieval process because it is well suited for long-term prediction and has a solid theoretical basis. The results show that the RMSE at station SC02 decreased by 2.855%, 17.519% and 15.756% compared to the nearby tide gauges, and the MAE decreased by 12.655%, 18.778% and 11.934% compared to the CM. This indicates that the inversion values in the near-coastal region have better robustness with the increasing elevation angle. The method contributes to the near-coastal sea level height monitoring.

In conclusion, residual sequences derived from SNR measurements hold promise as effective characteristics for sea level height monitoring, complementing existing inversion methods beyond spectral analysis. This advancement is poised to significantly enhance the development of GNSS-based infrastructure for monitoring sea surface and its scientific applications. The integration of deep learning into environmental monitoring, particularly in sea level height retrieval, offers the potential to enhance accuracy, streamline data analysis and reduce manual effort. Leveraging deep learning models enables researchers to achieve outstanding performance and glean valuable insights into environmental dynamics. Moreover, this approach holds promise for broader applications in diverse domains, such as monitoring soil moisture content and estimating snow depth, paving the way for more comprehensive environmental monitoring strategies, which is worth studying as a future direction.

Author Contributions: Conceptualization, A.T.; Methodology, A.T., X.Y. and Y.H.; Funding acquisition, Y.H. and W.L.; Projection administration, W.L., J.W. and Y.H.; Writing—original draft, A.T.; Writing—review and editing, Y.H., W.L., Q.Y. and A.T. All authors have read and agreed to the published version of the manuscript.

Funding: The research was funded by the National Natural Science Foundation of China under Grant (52071199).

Data Availability Statement: On request, simulated data can be made available. Station SC02's observations were collected via UNAVCO, while NOAA (https://tidesandcurrents.noaa.gov/waterlevels.html?id=9449880&type=Tide+Data&name=Friday%20Harbor&state=WA accessed on 1 October 2022) maintains the co-located tide gauge for SC02 station.

Acknowledgments: The authors additionally acknowledge the PBO Observation Program of the United States for supplying the GNSS data and International GNSS Service, as well as NOAA for providing in situ tidal gauge data for comparative analysis.

Conflicts of Interest: The authors declare no conflicts of interest.

References

1. Soulat, F.; Caparrini, M.; Germain, O.; Lopez-Dekker, P.; Taani, M.; Ruffini, G. Sea state monitoring using coastal GNSS-R. *Geophys. Res. Lett.* **2004**, *31*. [CrossRef]
2. Bevis, M.; Businger, S.; Herring, T.A.; Rocken, C.; Anthes, R.A.; Ware, R.H. GPS meteorology: Remote sensing of atmospheric water vapor using the global positioning system. *J. Geophys. Res. Atmos.* **1992**, *97*, 15787–15801. [CrossRef]
3. Wickert, J.; Cardellach, E.; Martín-Neira, M.; Bandeiras, J.; Bertino, L.; Andersen, O.B.; Camps, A.; Catarino, N.; Chapron, B.; Fabra, F. GEROS-ISS: GNSS reflectometry, radio occultation, and scatterometry onboard the international space station. *IEEE J. Sel. Top. Appl. Earth Obs. Remote Sens.* **2016**, *9*, 4552–4581. [CrossRef]
4. Larson, K.M.; Ray, R.D.; Nievinski, F.G.; Freymueller, J.T. The accidental tide gauge: A GPS reflection case study from Kachemak Bay, Alaska. *IEEE Geosci. Remote Sens. Lett.* **2013**, *10*, 1200–1204. [CrossRef]
5. Yan, Q.; Liu, S.; Chen, T.; Jin, S.; Xie, T.; Huang, W. Mapping Surface Water Fraction Over the Pan-tropical Region Using CYGNSS Data. *IEEE Trans. Geosci. Remote Sens.* **2024**, *62*, 5800914. [CrossRef]
6. Larson, K.M.; Nievinski, F.G. GPS snow sensing: Results from the EarthScope Plate Boundary Observatory. *GPS Solut.* **2013**, *17*, 41–52. [CrossRef]
7. Larson, K.M.; Small, E.E.; Gutmann, E.; Bilich, A.; Axelrad, P.; Braun, J. Using GPS multipath to measure soil moisture fluctuations: Initial results. *GPS Solut.* **2008**, *12*, 173–177. [CrossRef]
8. Yan, Q.; Huang, W. Sea ice thickness measurement using spaceborne GNSS-R: First results with TechDemoSat-1 data. *IEEE J. Sel. Top. Appl. Earth Obs. Remote Sens.* **2020**, *13*, 577–587. [CrossRef]
9. Yan, Q.; Huang, W. Sea ice remote sensing using GNSS-R: A review. *Remote Sens.* **2019**, *11*, 2565. [CrossRef]

10. Jackson, T.J.; Chen, D.; Cosh, M.; Li, F.; Anderson, M.; Walthall, C.; Doriaswamy, P.; Hunt, E.R. Vegetation water content mapping using Landsat data derived normalized difference water index for corn and soybeans. *Remote Sens. Environ.* **2004**, *92*, 475–482. [CrossRef]
11. Martin-Neira, M. A passive reflectometry and interferometry system (PARIS): Application to ocean altimetry. *ESA J.* **1993**, *17*, 331–355.
12. Anderson, K.D. Determination of water level and tides using interferometric observations of GPS signals. *J. Atmos. Ocean. Technol.* **2000**, *17*, 1118–1127. [CrossRef]
13. Limsupavanich, N.; Guo, B.; Fu, X. Application of RNN on GNSS Reflectometry Sea level monitoring. *Int. J. Remote Sens.* **2022**, *43*, 3592–3608. [CrossRef]
14. Kim, S.-K.; Park, J. Monitoring a storm surge during Hurricane Harvey using multi-constellation GNSS-Reflectometry. *GPS Solut.* **2021**, *25*, 63. [CrossRef]
15. Raj, N.; Brown, J. Prediction of Mean Sea Level with GNSS-VLM Correction Using a Hybrid Deep Learning Model in Australia. *Remote Sens.* **2023**, *15*, 2881. [CrossRef]
16. Jian, L.; Wang, X.; Huang, S.; Hao, H.; Zhang, X.; Yang, X. Comparative analysis of different empirical mode decomposition-kind algorithms on sea-level inversion by GNSS-MR. *J. Appl. Geod.* **2024**, *18*, 133–152. [CrossRef]
17. Hu, Y.; Yuan, X.; Liu, W.; Wickert, J.; Jiang, Z. GNSS-R snow depth inversion based on variational mode decomposition with multi-GNSS constellations. *IEEE Trans. Geosci. Remote Sens.* **2022**, *60*, 2005512. [CrossRef]
18. Williams, S.; Nievinski, F. Tropospheric delays in ground-based GNSS multipath reflectometry—Experimental evidence from coastal sites. *J. Geophys. Res. Solid Earth* **2017**, *122*, 2310–2327. [CrossRef]
19. Nievinski, F.G.; Larson, K.M. Forward modeling of GPS multipath for near-surface reflectometry and positioning applications. *GPS Solut.* **2014**, *18*, 309–322. [CrossRef]
20. Lomb, N.R. Least-squares frequency analysis of unequally spaced data. *Astrophys. Space Sci.* **1976**, *39*, 447–462. [CrossRef]
21. Larson, K.M.; Gutmann, E.D.; Zavorotny, V.U.; Braun, J.J.; Williams, M.W.; Nievinski, F.G. Can we measure snow depth with GPS receivers? *Geophys. Res. Lett.* **2009**, *36*, L17502. [CrossRef]
22. Yu, K.; Ban, W.; Zhang, X.; Yu, X. Snow depth estimation based on multipath phase combination of GPS triple-frequency signals. *IEEE Trans. Geosci. Remote Sens.* **2015**, *53*, 5100–5109. [CrossRef]
23. Chen, Q.; Won, D.; Akos, D.M. Snow depth sensing using the GPS L2C signal with a dipole antenna. *EURASIP J. Adv. Signal Process.* **2014**, *2014*, 106. [CrossRef]
24. Qian, X.; Jin, S. Estimation of snow depth from GLONASS SNR and phase-based multipath reflectometry. *IEEE J. Sel. Top. Appl. Earth Obs. Remote Sens.* **2016**, *9*, 4817–4823. [CrossRef]
25. Zheng, N.; Chen, P.; Li, Z. Accuracy analysis of ground-based GNSS-R sea level monitoring based on multi GNSS and multi SNR. *Adv. Space Res.* **2021**, *68*, 1789–1801. [CrossRef]
26. Zheng, N.; Chen, P.; Li, Z.; Ma, Y.; Liu, L. Tide height inversion and accuracy analysis based on GNSS-MR technology. In Proceedings of the China Satellite Navigation Conference (CSNC) 2020 Proceedings: Volume I, Chengdu, China, 23–25 May 2020; pp. 141–152.
27. Zhang, S.; Liu, K.; Liu, Q.; Zhang, C.; Zhang, Q.; Nan, Y. Tide variation monitoring based improved GNSS-MR by empirical mode decomposition. *Adv. Space Res.* **2019**, *63*, 3333–3345. [CrossRef]
28. Böhm, J.; Möller, G.; Schindelegger, M.; Pain, G.; Weber, R. Development of an improved empirical model for slant delays in the troposphere (GPT2w). *GPS Solut.* **2015**, *19*, 433–441. [CrossRef]
29. Bennett, G. The calculation of astronomical refraction in marine navigation. *J. Navig.* **1982**, *35*, 255–259. [CrossRef]
30. Peng, D.; Hill, E.M.; Li, L.; Switzer, A.D.; Larson, K.M. Application of GNSS interferometric reflectometry for detecting storm surges. *GPS Solut.* **2019**, *23*, 47. [CrossRef]
31. Fang, W.; Jiang, J.; Lu, S.; Gong, Y.; Tao, Y.; Tang, Y.; Yan, P.; Luo, H.; Liu, J. A LSTM algorithm estimating pseudo measurements for aiding INS during GNSS signal outages. *Remote Sens.* **2020**, *12*, 256. [CrossRef]
32. Lindsey, J. The Fresnel zone and its interpetive significance. *Lead. Edge* **1989**, *8*, 33–39. [CrossRef]
33. Bayındır, C.; Altintas, A.A.; Ozaydin, F. Self-localized solitons of a q-deformed quantum system. *Commun. Nonlinear Sci. Numer. Simul.* **2021**, *92*, 105474. [CrossRef]
34. Xu, H.; Wu, H. Accurate tsunami wave prediction using long short-term memory based neural networks. *Ocean. Model.* **2023**, *186*, 102259. [CrossRef]
35. Meng, Z.-F.; Chen, Z.; Khoo, B.C.; Zhang, A.-M. Long-time prediction of sea wave trains by LSTM machine learning method. *Ocean. Eng.* **2022**, *262*, 112213. [CrossRef]

Disclaimer/Publisher's Note: The statements, opinions and data contained in all publications are solely those of the individual author(s) and contributor(s) and not of MDPI and/or the editor(s). MDPI and/or the editor(s) disclaim responsibility for any injury to people or property resulting from any ideas, methods, instructions or products referred to in the content.